Materials Research Letters

ISSN: 2166-3831 (Online) Journal homepage: www.tandfonline.com/journals/tmrl20

Realizing superior strength-ductility combination in dual-phase AlFeCoNiV high-entropy alloy through composition and microstructure design

Zhenhua Ye, Chuanwei Li, Mengyao Zheng, Xinyu Zhang, Xudong Yang, Qing Wang & Jianfeng Gu

To cite this article: Zhenhua Ye, Chuanwei Li, Mengyao Zheng, Xinyu Zhang, Xudong Yang, Qing Wang & Jianfeng Gu (2022) Realizing superior strength-ductility combination in dual-phase AlFeCoNiV high-entropy alloy through composition and microstructure design, Materials Research Letters, 10:11, 736-743, DOI: 10.1080/21663831.2022.2093140

To link to this article: https://doi.org/10.1080/21663831.2022.2093140

© 2022 The Author(s). Published by Informa UK Limited, trading as Taylor & Francis Group

Published online: 03 Jul 2022.

Submit your article to this journal

Article views: 5255

View related articles

View Crossmark data

Citing articles: 47 View citing articles

Full Terms & Conditions of access and use can be found at
https://www.tandfonline.com/action/journalInformation?journalCode=tmrl20

MATER. RES. LETT.
2022, VOL. 10, NO. 11, 736–743
https://doi.org/10.1080/21663831.2022.2093140

MATERIALS RESEARCH LETTERS
Taylor & Francis
Taylor & Francis Group

ORIGINAL REPORTS

OPEN ACCESS
Check for updates

Realizing superior strength-ductility combination in dual-phase AlFeCoNiV high-entropy alloy through composition and microstructure design

Zhenhua Ye[a], Chuanwei Li[a], Mengyao Zheng[a], Xinyu Zhang[a], Xudong Yang[a], Qing Wang[b] and Jianfeng Gu[a,c]

[a]Institute of Materials Modification and Modelling, School of Materials Science and Engineering, Shanghai Jiao Tong University, Shanghai, People's Republic of China; [b]Laboratory for Microstructures, Institute of Materials, Shanghai University, Shanghai, People's Republic of China; [c]Shanghai Key Laboratory of Materials Laser Processing and Modification, Shanghai Jiao Tong University, Shanghai, People's Republic of China

ABSTRACT

Achieving high strength and ductility simultaneously in high-entropy alloys (HEAs) has always been a challenge, and recent studies indicate that duplex microstructure provides a strategy to solve this contradiction. We prepared $Al_{0.25}FeCoNiV$ HEA with $L1_2$/B2 fine-grain duplex microstructure and achieved a remarkable combination of the ultimate tensile strength (1530 MPa) and ductility (20%), which clearly outperforms other duplex HEAs. Owing to the formation of fine-grain microstructure and the hindrance of the B2 phase, high yield strength has been achieved. Furthermore, the excellent work-hardening ability of the $L1_2$ phase and the dispersion of the B2 phase ensured uniform deformation and high strength.

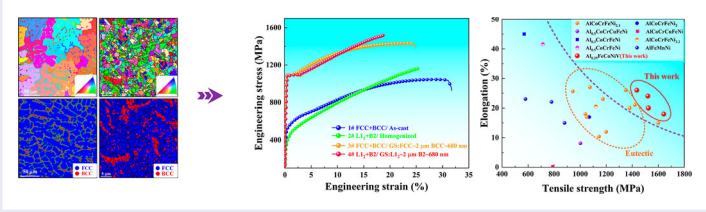

IMPACT STATEMENT

$Al_{0.25}FeCoNiV$ HEAs exhibit a remarkable combination of ultimate tensile strength and ductility through $L1_2$/B2 fine-grain duplex microstructure, which clearly outperforms other duplex HEAs.

ARTICLE HISTORY
Received 28 January 2022

KEYWORDS
High-entropy alloys; dual-phase microstructure; strength–ductility trade-off

Introduction

High-entropy alloys (HEAs), a new type of alloys with more than four principal elements in equal or nearly equal atomic percentages, have attracted increasing attention owing to their unique microstructure and properties; for example, HEAs with body centered cubic (BCC) structure exhibit high strength and those with face centered cubic (FCC) structure exhibit high ductility [1–3]. However, nearly 10 years of research have shown that it is difficult to overcome the strength–ductility trade-off in single-phase HEAs [4]. Fortunately, the microstructures and mechanical properties of HEAs were found and can be tuned by modifying the chemical composition and thermal processes. Recent studies suggest that a dual-phase structure is effective in improving the mechanical properties of HEAs. For instance, Li et al. [5] demonstrated that the strength–ductility trade-off in metastable dual-phase $Fe_{50}Mn_{30}Co_{10}Cr_{10}$ alloys can be resolved by varying the Mn content to generate transformation-induced plasticity (TRIP). Lu et al. [6] proposed a eutectic HEA with FCC/BCC lamellar structure, $AlCoCrFeNi_{2.1}$, which combines the advantages of BCC and FCC phases. Furthermore, Shi et al. [7,8] obtained ultrafine-grain microstructure through heavy cryorolling and annealing, which exhibited ultimate tensile strength (UTS) of 1.6 GPa and ductility of 14%. However, the design of dual-phase alloy systems that exhibit TRIP or eutectic lamellar structure is still a challenge because the complex composition makes it difficult to predict the microstructure, often requiring several trial-and-error experiments.

CONTACT Chuanwei Li li-chuanwei@sjtu.edu.cn Institute of Materials Modification and Modelling, School of Materials Science and Engineering, Shanghai Jiao Tong University, Shanghai 200240, People's Republic of China; Jianfeng Gu gujf@sjtu.edu.cn Institute of Materials Modification and Modelling, School of Materials Science and Engineering, Shanghai Jiao Tong University, Shanghai 200240, People's Republic of China

© 2022 The Author(s). Published by Informa UK Limited, trading as Taylor & Francis Group
This is an Open Access article distributed under the terms of the Creative Commons Attribution License (http://creativecommons.org/licenses/by/4.0/), which permits unrestricted use, distribution, and reproduction in any medium, provided the original work is properly cited.

Previous reports suggest that FCC/BCC dual-phase structure can be obtained by adding Al in FCC-structured HEAs, and the amount of BCC phase can be controlled within a certain range [9–12]. This is based on the research of the valence electron concentration (VEC) effect on the phase stability in solid solution forming HEAs, BCC phases are stabilized at a lower VEC (< 6.87), while FCC phases are stabilized at a higher VEC (> 8.0), and in the intermediate VEC (6.87 < VEC < 8.0), both FCC and BCC phases exist [13]. Although the introduction of the BCC phase improves the mechanical properties, a low amount causes limited enhancement in the strength, and a high amount makes the alloy brittle. For example, Li et al. prepared $Al_{0.3}FeCoCrNiMn$ HEA with ultrafine microstructure through severe cold rolling and annealing treatment and then achieved yield strength (YS) of 1 GPa, but with low strain-hardening ability and plasticity less than 10% [14]. In addition, other hard and brittle phases, such as the σ phase, may form during the annealing process with the increase of Al contents [14]. Thus, it is difficult to achieve strength–ductility balance in HEAs through this strategy in current studies.

Vanadium (V) is an optimal element for strengthening FCC high-entropy alloys, and V is a key element in improving the Hall-Petch coefficient to enhance yield strength, such as CoNiV and $V_{10}Cr_{15}Mn_5Fe_{35}Co_{10}Ni_{25}$ HEAs [15,16]; Meanwhile, V is easy to form intermetallic compounds and reducing the V content can effectively avoid the generation of intermetallic phases [17]. Hence, an equiatomic single-phase FeCoNiV HEA with FCC-$L1_2$ phase transition occurring at approximately 785°C was selected as the base alloy. The VEC of the Al element is very low, only 3. Therefore, the introduction of the Al element can reduce the VEC of the system and promote the transformation from FCC to BCC phase. In this paper, we introduced Al in FeCoNiV HEAs to control the VEC of the system and design an FCC/BCC duplex microstructure.

Materials and methods

The $Al_{0.25}FeCoNiV$, referred to as Al025 was fabricated by arc melting under a high-purity argon atmosphere. The purities of all the elements are $\geq$ 99.95 wt. %. The liquid-state alloys were cast into a copper mold with dimensions of $7 \times 10 \times 100\,mm^3$, samples taken from this state are denoted as 1#. The ingots were homogenized at 1100°C for 10 h in an argon-protected environment and cooled to room temperature with the furnace (2#). Then the ingots were cold-rolled at room temperature with a reduction ratio of 90% (thickness: 1 mm). Subsequent recrystallization and annealing treatments were performed in quartz ampules, which were then water quenched. Samples subjected to recrystallization at 900°C for 1.5 h are denoted as 3#. The samples subsequently annealed at 755°C for 10 min are named 4#.

The thermal properties of the HEAs were investigated by differential scanning calorimetry (DSC) with 96 Line equipment (SETARAM instrumentation, France) operated in a N_2 atmosphere from 50 to 1100°C at a rate of 10°C/min. The different phases in the HEAs were determined by X-ray diffraction (XRD; D8 ADVANCE Da Vinci, Bruker, Germany) and Synchrotron radiation X-ray diffraction (SXRD; BL14B1 beamline of Shanghai Synchrotron Radiation Facility, China). The phase characterization and deformation behavior were investigated using energy disperse spectroscopy (EDS), electron backscatter diffraction (EBSD), and transmission electron microscopy (TEM). The EBSD and EDS investigations were performed in a scanning electron microscope (SEM; LYRA3 GMU, TESCAN, Czech Republic). The TEM and EDS investigations were performed using a JEM-2100F (JEOL, Japan) instrument at an accelerating voltage of 200 kV. The samples for TEM analysis were prepared by conventional electropolishing of foils (mechanically pre-thinned to 60 μm) in a mixture of 10% $HClO_4$ and 90% C_2H_5OH at 25 V and −25°C. Tensile tests were performed using a universal testing machine (MTEST 5000 W Tensile Stage, GATAN, UK) at a quasi-static strain rate of 0.1 mm/min and room temperature. Plate-type tensile specimens (gauge length: 4 mm, cross-section: $1 \times 2\,mm^2$) fabricated by electrical discharge machining were used for the tensile tests. The strain was measured synchronously during the tensile process by digital image correlation using Vic-2D software (Correlated Solutions, USA). For this, a speckle pattern was applied on the surface of the tensile specimens.

Results and discussion

The DSC curves of the as-cast HEAs in Figure 1(a) show that the exothermic and endothermic peaks in the heating and cooling processes of Al025 HEA, respectively. And this phenomenon corresponds to the solid-state phase transformation of the studied alloy. The XRD results of the as-cast HEAs confirm that the addition of Al promotes the formation of the BCC phase, and Al025 exhibits the FCC/BCC dual-phase structure as shown in Figure 1(b). And no phase transition can be seen between as-cast (1#) and homogenized state (2#). Detail investigation on the microstructure including EBSD and TEM analysis was carried out and 1# Al025 HEA exhibits a dual-phase microstructure consisting of FCC and BCC phases; the fraction of the BCC phase is 12 vol.%, as shown in Figure 1(c–f). The BCC phase is distributed

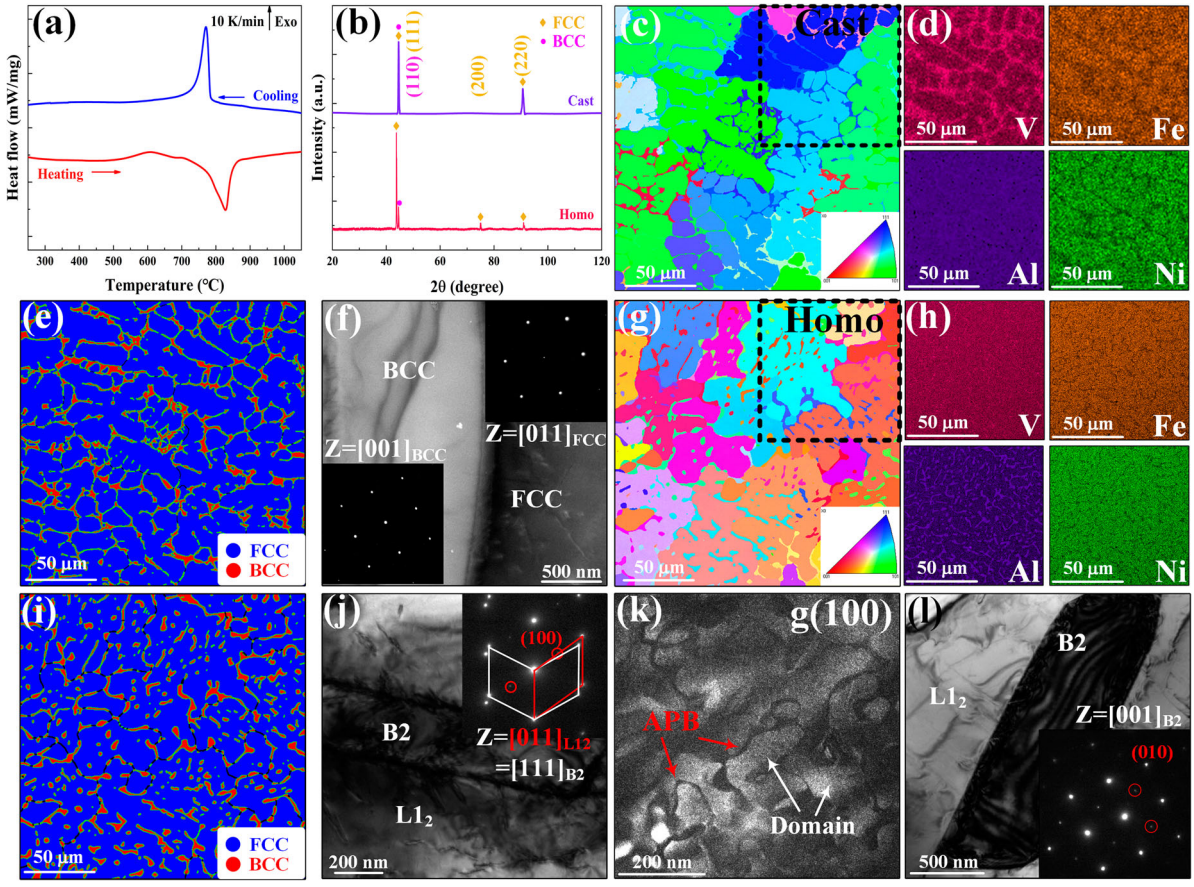

Figure 1. (a) DSC heating and cooling curves, (b) XRD patterns of as-cast (1#) and homogenized (2#) Al025 HEAs; (c)–(f) grain orientation map, EDS maps, phase distribution map and bright-field (BF) image with selected area electron diffraction (SAED) pattern of 1# Al025 HEA; (g)–(l) grain orientation map, EDS maps, phase distribution map and BF image with SAED pattern, dark-field (DF) image corresponding to superlattice spot (100) of $L1_2$ phase, BF image and SAED pattern along B2 phase [001] zone axis of 2# Al025 HEA.

at the grain boundaries and the interdendritic regions of the FCC phase, and there seems to be an orientation relationship between the BCC phase and the FCC phase. The V content (28.80%) in the BCC phase is significantly higher than that in the FCC phase (21.80%). After homogenization treatment, Al025 still exhibits duplex microstructure and component dendrites were eliminated. The Al content (13.50%) in the BCC phase is evidently higher than that in the FCC phase (4.30%) (Figure 1(g–i)). The detailed chemical compositions of the HEAs are presented in Table 1. It is important that the FCC and BCC phases in the 2# sample are found to translate to chemical ordered $L1_2$ and B2 phases, respectively, from the TEM studies (Figure 1(j–l)). And the dark-field (DF) image corresponding to the superlattice spot (100) of the $L1_2$ phase shows clear anti-phase boundaries (APBs) and domain structure. The orientation relationship is not affected, and the orientation of the partial two phases still satisfies the K–S relationship ($\{111\}_{L12}//\{110\}_{B2}; \langle 1\bar{1}0\rangle_{L12}//\langle 1\bar{1}1\rangle_{B2}$).

Figure 2 shows the detailed microstructures of the recrystallized (3#) and subsequent annealed (4#) Al025 HEAs. The SXRD results (Figure 2(a)) show that after cold-rolling and recrystallization treatments, Al025 alloy exhibited the FCC/BCC dual-phase structure, annealed Al025 alloy was composed of $L1_2$ phase and B2 phase, and no other intermetallic compounds were observed. The 3# Al025 HEA exhibits a fine-grain dual-phase microstructure and similar element distribution inhomogeneous, as shown in Figure 2(b–d). The average grain size of the $L1_2$ phase is approximately 2 μm, while that of

Table 1. Chemical composition (at. %) of these HEAs as determined by SEM/TEM-EDS analysis.

Alloy	Samples	Phase	Al	Fe	Co	Ni	V
Al025FeCoNiV	As-cast (1#)	Overall	5.80	23.40	23.80	23.00	24.00
		FCC	5.50	24.60	24.40	23.70	21.80
		BCC	7.50	22.70	22.50	18.60	28.80
	Homogenized	$L1_2$	4.30	24.30	23.90	23.70	23.80
	(2#)	B2	13.50	20.60	23.30	18.30	24.30
	3#	FCC	3.62	26.38	23.68	23.09	23.23
		BCC	15.95	21.76	23.43	15.47	23.38
	4#	$L1_2$	3.62	26.38	23.68	23.09	23.23
		B2	15.95	21.76	23.43	15.47	23.38

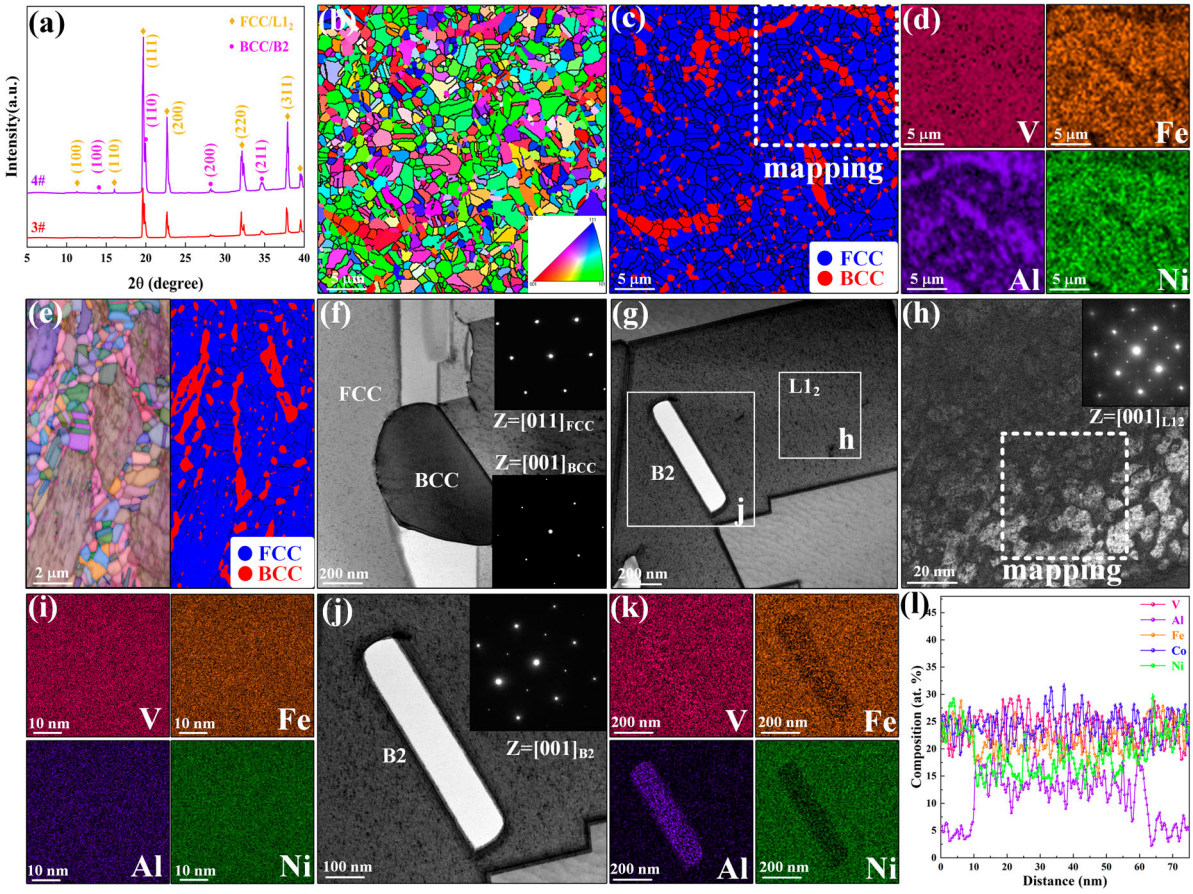

Figure 2. (a) SXRD patterns of recrystallized (3#) and annealed states (4#) Al025 HEAs; (b)–(d) grain orientation map, phase distribution map and EDS maps of Al025 HEA recrystallized at 900°C for 1.5 h (3#); (e) Euler distribution map and phase distribution map of Al025 HEA recrystallized at 800°C for 10 h; (f) BF image with SAED pattern of 3# Al025 HEA; (g)–(l) BF image. DF image corresponding to (100) of $L1_2$ phase with SAED pattern along $L1_2$ [001] zone axis, TEM-EDS maps of $L1_2$ region, BF image with SAED pattern along B2 [001] zone axis, TEM-EDS maps of B2 region and EDS composition profiles across B2 phase of 4# Al025 HEA.

the B2 phase is approximately 680 nm. The phase distribution map (Figure 2(c)) shows that there are two types of B2 phases: one consisting of large clusters (approximately 1 μm), and the other consisting of small grains (approximately 200 nm) dispersed on the $L1_2$ grain boundaries and inside the $L1_2$ grain. The EDS maps in Figure 2(d) show that the Al element distributes differently between B2 and $L1_2$ phases, whereas the distribution of V in the two phases is relatively uniform. In addition, the two types of B2 phases have similar compositions. When the recrystallization temperature is decreased to 800°C, it is found that the $L1_2$ phase is partially recrystallized while the B2 phase is completely recrystallized, as shown in Figure 2(e). In particular, it is observed that there is a large number of recrystallized B2 grains in the non-recrystallized $L1_2$ region. This confirms that the B2 phase is more likely to nucleate and recrystallize in the recrystallization process, and it seems difficult to grow up, which then can pin $L1_2$ grain boundaries and refine the $L1_2$ grains. The EBSD and TEM results indicate a dual-phase microstructure consisting of FCC and BCC phases and there is no orientation relationship, especially between the BCC phase and the FCC phase (Figure 2(b,f)). After annealing at 755°C for 10 min, the 4# Al025 HEA exhibits a fine-grain dual-phase microstructure consisting of $L1_2$ and B2 phases, as shown in Figure 2(g). And the dark-field (DF) image corresponding to the superlattice spot exhibits irregular ordered domain structure, and combined with TEM-EDS, a single $L1_2$ phase was confirmed in this region (Figure 2(h,i)). B2 phase was also confirmed in this way and TEM-EDS reveals its characteristics of rich Al and poor Ni elements (Figure 2(j–l)).

Figure 3 shows the tensile properties of these HEAs at room temperature. The YS of fine grains 3# and 4# Al025 HEA (1100 MPa) is significantly higher than that of coarse grains 1# and 2# Al025 HEA; it is even higher than the ultimate tensile strength of 1# HEA, as shown in Table 2. In contrast to 3#, 4# Al025 HEA exhibits little improvement in the YS owning to the

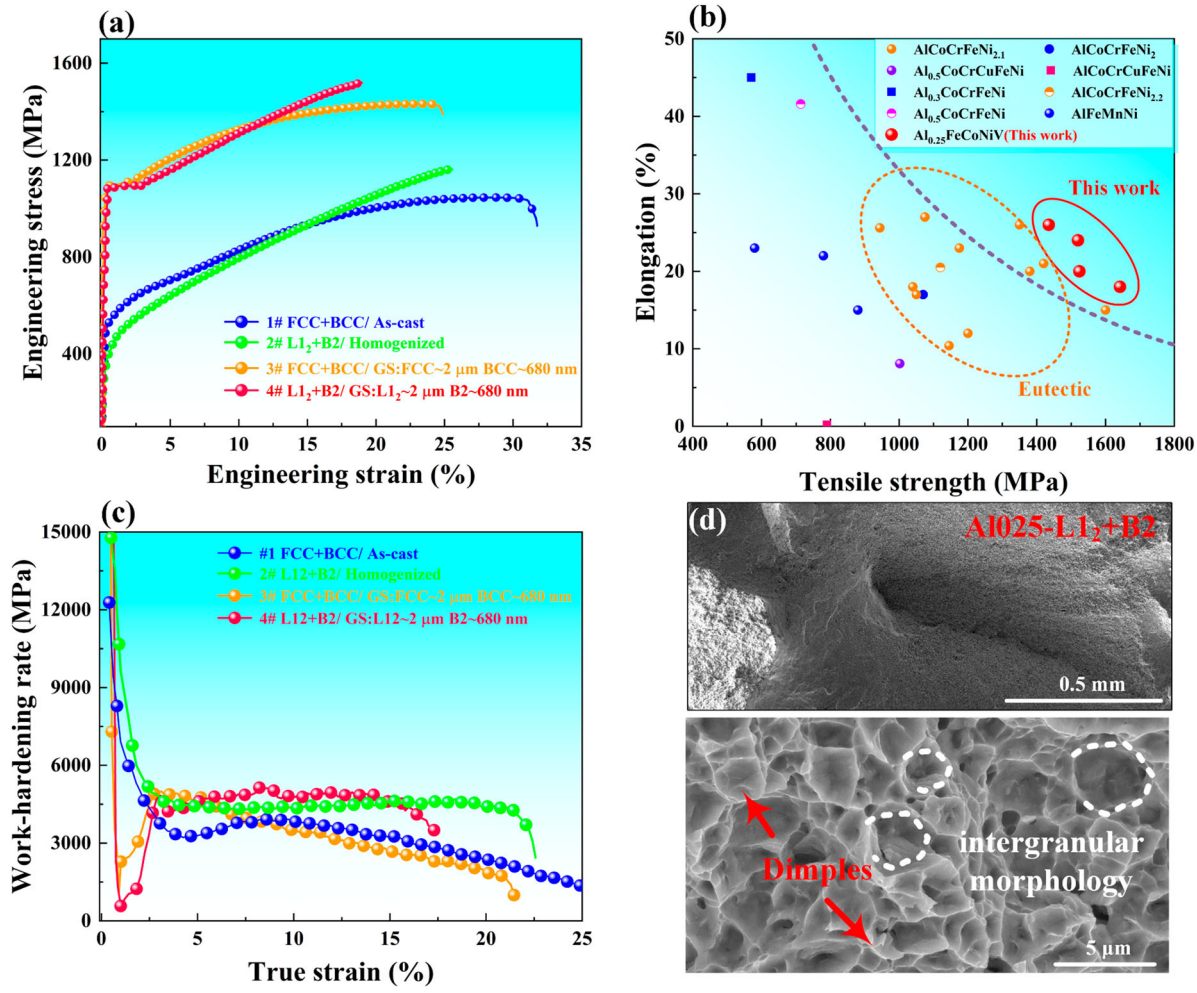

Figure 3. (a) Tensile engineering stress–strain curves, (b) comparison of the mechanical properties of Al025 HEA with those of existing dual-phase HEAs, (c) strain-hardening rate curves, (d) SEM images of the fracture surfaces of 4# Al025 HEA.

Table 2. YS, UTS, and uniform strain (US) of Al025 HEAs.

Alloy	YS (MPa)	UTS (MPa)	US (%)
1#	510	1045	30
2#	420	1161	25
3#	1087	1430	25
4#	1098	1530	19

ordered structure of $L1_2$ and B2 phase, while the tensile strength increases from 1430 to 1530 MPa with little loss of ductility. Compared with 1# samples with disordered structure, 2# samples also have a similar trend. Figure 3(b) directly compares the mechanical properties (tensile strength/elongation) of typical FCC/BCC duplex phase HEAs. The solid orange dots in the figure represent the mechanical properties of typical FCC/BCC eutectic systems of $AlCoCrFeNi_{2.1}$ HEAs, including the results of ultrafine duplex microstructures obtained through deformation control by Shi et al. [7]. it is evident that this Al025 HEA exhibits the best mechanical properties [6,7,14,18–21]. To elucidate the strengthening and deformation mechanisms of Al025 HEA, the work-hardening rate was analyzed as a function of the plastic strain, as shown in Figure 3(c). First, by comparing the work-hardening curves of 2# and 4#, grain size and B2 phase distribution have an influence on the early stage of the strain-hardening process and have little effect on the subsequent strain-hardening behavior. Second, the excellent work-hardening ability in 2# and 4# Al025 HEAs should be attributed to the ordered structure of the $L1_2$ and B2 phase by contrast with the disordered structure of Al025 HEAs. According to the previous studies on ordered alloys [22–26], both the $L1_2$ phase and B2 phase have been reported to improve work-hardening rate, which is related to the superdislocations configuration and slip behavior. Third, because of the previous synthesis effect, a homogeneous deformation can be maintained and good ductility is expected in the Al025 alloy. The representative fracture surfaces of 4# Al025 HEAs are shown in Figure 3(d). The fracture is almost ductile dimple fracture, which is due to the considerable deformation capacity of the $L1_2$ phase [27]. The fracture morphology

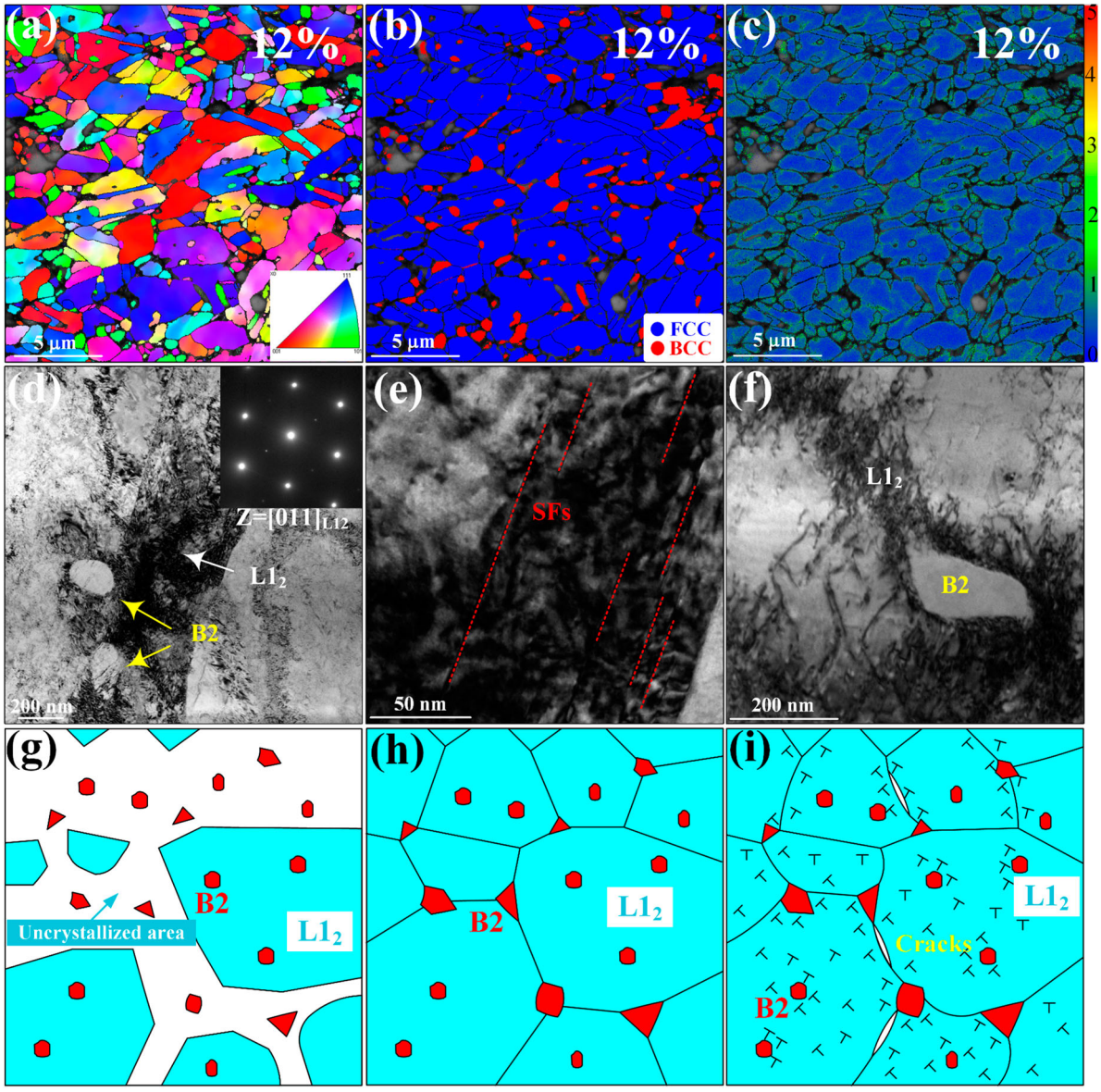

Figure 4. (a)–(c) Grain orientation map, phase map, and KAM map of 4# Al025 HEA subjected to strain of 12%; (d)–(f) BF image along L12 [011] zone axis of 4# sample; (g)–(i) Schematic of the recrystallization and deformation processes in 4# Al025 HEA.

also includes intergranular facets marked by white dotted lines, with a size of less than 3 μm, which is consistent with the grain size of the $L1_2$ phase. In addition, there are dark holes near the intergranular facets, and the size is consistent with B2 on the grain boundary.

To further investigate the deformation behavior in the fine-grain dual-phase HEA, detailed characterizations were carried out on the 4# Al025 HEA sample. Figure 4(a)–(c) shows the EBSD inverse pole figure, phase map, and kernel average misorientation (KAM) distribution map of the 4# Al025 HEA subjected to a strain of 12% at room temperature. According to the definition of KAM, a low KAM value indicates homogeneous plastic deformation among the local regions. The $L1_2$ phase bears the main strain, while the strain gradient is mainly distributed within the B2 phase and the interface between $L1_2$ and B2 phases. Predictably, the stress accumulated in the phase boundaries between the B2 phase and $L1_2$ phase cannot be released because of the limited deformation ability, and cracks can easily initiate along the phase boundaries. Further TEM investigations were shown in Figure 4(d–f) to reveal the deformation mechanism in B2 and $L1_2$ phases. Figure 4(d) shows the BF image and SAED along the $L1_2$ [011] zone axis of 4# Al025 HEA. A large number of dislocations were found distributed in the $L1_2$ phase and little dislocations can be seen in the B2 phase. SAED results indicate the existence of stacking faults (SFs) and lots of SFs can be seen in the $L1_2$ phase, as

shown in Figure 4(e). The deformation ability of the $L1_2$ phase in Al025 HEA is stronger than that of traditional $L1_2$ phases, such as Ni_3Al and Ni_3Si; and the current widely accepted explanation of strain hardening is that the special jogs generated by dislocation intersection or cross-slip bring additional hardening reported in Cu_3Au and $(Fe, Co, Ni)_3V$ [23,24,28,29]. According to the previous studies and the current results [27], we believe that $L1_2$ phase phases have a dominant role in the straightforward hardening and the deformation mechanism of the $L1_2$ phase in Al025 HEA needs to be studied further. The present work mainly focuses on the deformation ability of the B2 phase and the interface between the $L1_2$ and B2 phases, since the introduction of the B2 phase in AlFeCoNiV HEA affects the plasticity of the material. As shown in Figure 4(f), abundant dislocation pile-up at the interface between the $L1_2$ and B2 phases, reflects the influence of the B2 phase on the strength and plasticity.

The evolution of the dual-phase microstructure in Al025 during heat treatment and deformation is summarized in Figures 4(g–i), which explains the origin of strength and plasticity. The grains of the $L1_2$ phase is relatively large in the homogenized sample (2#), and the B2 phase is distributed at the grain boundaries and inside the grains. The BCC phase is crushed by cold-rolling deformation, and the nucleation of the BCC phase is superior to that of the FCC phase in the subsequent recrystallization process. This results in microstructure refinement as shown in Figure 4(g,h). The hindrance of the B2 phase on the dislocation slip also contributes to the YS. Moreover, since V can significantly improve the Hall-Petch coefficient, the pinning of $L1_2$ grain boundaries by the BCC phase to obtain fine grains can significantly improve the YS of Al025 alloys, which is different from previous dual-phase HEAs. The $L1_2$ phase plays an important role in the strain-hardening process, and deformation mainly occurs in the $L1_2$ phase, as shown in Figure 4(i). However, as deformation progresses, the deformation of the phase boundaries and that of the grain boundaries between B2 grains are not synchronized owing to the poor deformation ability of the B2 phase. This results in an intergranular fracture which is confirmed by the fracture surface. Increasing the deformation of the BCC phase during the cold rolling process to obtain a more dispersed BCC phase is beneficial for further improving the mechanical properties of these AlFeCoNiV HEAs.

In summary, high strength–ductility combination was achieved in Al025 HEA with an $L1_2$/B2 fine-grain duplex microstructure via the coordination of $L1_2$/B2 in the deformation process. The $L1_2$ phase is a prerequisite for plastic deformation, and fine grains significantly contribute to the YS owing to the high Hall-Petch coefficient. Moreover, the unique strain-hardening behavior of the $L1_2$ phase ensures uniform deformation of the material, and the dispersed B2 phase prevents direct expansion of the crack. The fine B2 phase (even though in small amounts) not only refines the $L1_2$ grains but also contributes to the YS. The role of the B2 phase in Al025 HEA is different from that in previously reported duplex-microstructure alloys. This finding is beneficial for designing a strategy to develop new duplex HEAs with outstanding strength–ductility combination.

Acknowledgement

The use of synchrotron radiation X-ray diffraction was supported by Shanghai Synchrotron Radiation Facility, China.

Disclosure statement

No potential conflict of interest was reported by the author(s).

Funding

This work was financially supported by the National Key Research and Development Program of China (grant number 2018YFA07029) and the National Natural Science Foundation of China (grant number 52171042, 51801126), and the China Postdoctoral Science Foundation (grant number 2020T130402).

References

[1] Yeh JW, Chen SK, Lin SJ, et al. Nanostructured high-entropy alloys with multiple principal elements: novel alloy design concepts and outcomes. Adv Eng Mater. 2004;6(5):299–303.
[2] Senkov ON, Wilks GB, Miracle DB, et al. Refractory high-entropy alloys. Intermetallics. 2010;18(9):1758–1765.
[3] Senkov ON, Wilks GB, Scott JM, et al. Mechanical properties of $Nb_{25}Mo_{25}Ta_{25}W_{25}$ and $V_{20}Nb_{20}Mo_{20}Ta_{20}W_{20}$ refractory high entropy alloys. Intermetallics. 2011;19(5): 698–706.
[4] Yi J, Yang L, Wang L, et al. Novel, equimolar, multi-phase CoCuNiTiV high-entropy alloy: phase component, microstructure, and compressive properties. Met Mater Int. 2021;27(7):2387–2394.
[5] Li Z, Pradeep KG, Deng Y, et al. Metastable high-entropy dual-phase alloys overcome the strength-ductility trade-off. Nature. 2016;534(7606):227–230.
[6] Lu Y, Dong Y, Guo S, et al. A promising new class of high-temperature alloys: eutectic high-entropy alloys. Sci Rep. 2014;4:6200.
[7] Shi P, Ren W, Zheng T, et al. Enhanced strength-ductility synergy in ultrafine-grained eutectic high-entropy alloys by inheriting microstructural lamellae. Nat Commun. 2019;10(1):489–497.
[8] Shi P, Zhong Y, Li Y, et al. Multistage work hardening assisted by multi-type twinning in ultrafine-grained heterostructural eutectic high-entropy alloys. Mater Today. 2020;41:62–71.
[9] Tong C-J, Chen M-R, Yeh J-W, et al. Mechanical performance of the Al x CoCrCuFeNi high-entropy alloy

system with multiprincipal elements. Metall Mater Trans A. 2005;36(5):1263–1271.
[10] Kao Y-F, Chen T-J, Chen S-K, et al. Microstructure and mechanical property of as-cast, -homogenized, and -deformed AlxCoCrFeNi ($0 \leq x \leq 2$) high-entropy alloys. J Alloys Compd 2009;488(1):57–64.
[11] Lu W, Luo X, Yang Y, et al. Effects of Al addition on structural evolution and mechanical properties of the CrCoNi medium-entropy alloy. Mater Chem Phys. 2019;238:121841.
[12] Lin L, Xian X, Zhong Z, et al. Microstructure stability and its influence on the mechanical properties of CrMnFeCoNiAl0.25 high entropy alloy. Met Mater Int. 2019;26(8):1192–1199.
[13] Guo S, Ng C, Lu J, et al. Effect of valence electron concentration on stability of fcc or bcc phase in high entropy alloys. J Appl Phys. 2011;109(10):103505.
[14] Li Z, Fu L, Peng J, et al. Effect of annealing on microstructure and mechanical properties of an ultrafine-structured Al-containing FeCoCrNiMn high-entropy alloy produced by severe cold rolling. Mater Sci Eng A. 2020;786:139446.
[15] Sohn SS, Kwiatkowski da Silva A, Ikeda Y, et al. Ultra-strong medium-entropy single-phase alloys designed via severe lattice distortion. Adv Mater. 2019;31(8):1807142.
[16] Asghari-Rad P, Sathiyamoorthi P, Bae JW, et al. Effect of grain size on the tensile behavior of V10Cr15Mn5Fe35Co 10Ni25 high entropy alloy. Mater Sci Eng A. 2019;744: 610–617.
[17] Salishchev GA, Tikhonovsky MA, Shaysultanov DG, et al. Effect of Mn and V on structure and mechanical properties of high-entropy alloys based on CoCrFeNi system. J Alloys Compd. 2014;591:11–21.
[18] Bhattacharjee T, Wani IS, Sheikh S, et al. Simultaneous strength-ductility enhancement of a nano-lamellar $AlCoCrFeNi_{2.1}$ eutectic high entropy alloy by cryo-rolling and annealing. Sci Rep. 2018;8(1):3276.
[19] Yang H, Li J, Pan X, et al. Nanophase precipitation and strengthening in a dual-phase $Al_{0.5}CoCrFeNi$ high-entropy alloy. J Mater Sci Technol. 2021;72:1–7.
[20] Li P, Wang A, Liu CT. Composition dependence of structure, physical and mechanical properties of FeCoNi(Mn Al)$_x$ high entropy alloys. Intermetallics. 2017;87: 21–26.
[21] Huang X, Dong Y, Lu S, et al. Effects of homogenized treatment on microstructure and mechanical properties of $AlCoCrFeNi_{2.2}$ near-eutectic high-entropy alloy. Acta Metal Sin. 2021;34(8):1079–1086.
[22] Kear BH. Cross slip, antiphase defects and work hardening in ordered Cu_3Au. Acta Metall. 1966;14(5):659–677.
[23] Kear BH. Dislocation configurations and work hardening in Cu_3Au crystals. Acta Metall. 1964;12(5):555–569.
[24] Liu CT, Inouye H. Control of ordered structure and ductility of (Fe, Co, Ni)$_3$V alloys. Metall Trans A. 1979;10(10):1515–1525.
[25] Matsuda M, Nishimoto T, Matsunaga K, et al. Deformation structure in ductile B2-type Zr–Co–Ni alloys with martensitic transformation. J Mater Sci. 2011;46(12): 4221–4227.
[26] Vidoz AE, Brown LM. On work-hardening in ordered alloys. Philos Mag. 1962;7(79):1167–1175.
[27] Ye Z, Li C, Zheng M, et al. In situ EBSD/DIC-based investigation of deformation and fracture mechanism in FCC- and L12-structured FeCoNiV high-entropy alloys. Int J Plast. 2022;152:103247.
[28] Liu CT, Stiegler JO. Ductile ordered intermetallic alloys. Science. 1984;226(4675):636–642.
[29] Wang S, Chen S, Jia Y, et al. FCC-L12 ordering transformation in equimolar FeCoNiV multi-principal element alloy. Mater Des. 2019;168:107648.